THE JOURNAL OF PHYSICAL CHEMISTRY C
A JOURNAL OF THE AMERICAN CHEMICAL SOCIETY

pubs.acs.org/JPCC

Article

Photo-Induced Charge Transfer of Fullerene and Non-Fullerene Conjugated Polymer Blends via Ab Initio Excited-State Dynamics

Amirhadi Alesadi, Wenjie Xia,* and Dmitri Kilin*

Cite This: J. Phys. Chem. C 2022, 126, 12015−12024

Read Online

ACCESS | Metrics & More | Article Recommendations | Supporting Information

ABSTRACT: Organic conjugated polymers (CPs) are promising candidates for organic photovoltaic (OPV) devices due to their unique tunable mechanical and optoelectronic performance. Over the last decade, optoelectronic properties of narrow band gap CPs as a blend with acceptor units are largely optimized, which leads to noticeable progress in OPV technology. However, their power conversion efficiency is still lower than their organic counterparts (i.e., silicon), limiting their practical usage. In this study, we employ ab initio molecular dynamics to explore photo-induced charge transfer (CT) of the diketopyrrolopyrrole-based polymer as a blend with non-fullerene (i.e., ITIC) and fullerene (i.e., PCBM) acceptor units. The results of charge carrier dynamics induced by selected photoexcitation show that hole density redistribution in space is much faster than electron relaxation. We track the relaxation rates of charge carriers over time, where the derivative of the difference between the rate of electron and hole implies the current density at zero voltage. This can be utilized to characterize the CT performance of CPs blended with different acceptor units. Relaxation rate results indicate that CP blend with ITIC promises a better PV performance, illustrating that the current computational approach opens the door to determine bulk heterojunctions' electronic performance for OPV devices and narrowing down the list of potential donor−acceptor candidates.

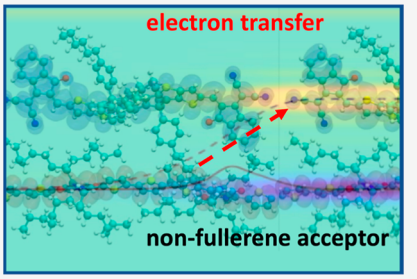

INTRODUCTION

Over the past decades, the development of semiconducting conjugated polymers (CPs)[1−6] provokes noticeable progress in organic photovoltaics (OPVs).[7−10] Generally, CPs are being utilized as a blend with acceptor units to form the bulk heterojunction (BHJ) for the active layer.[11] Currently, molecular engineering of CPs (i.e., donor) and acceptor units is one of the most important research directions to tune optoelectronic properties of OPVs, such as energy levels, absorption, and charge transfer (CT).[12−15] The rate of photo-induced CT at the interface of CPs and acceptors is a key parameter that characterizes the generation/recombination of charge carriers through a non-radiative process, determining the open-circuit voltage and attained power conversion efficiency (PCE). Despite tremendous efforts, organic OPVs are still under development because they are limited to lower PCE as opposed to their inorganic counterparts. Due to the endless possibilities of molecular modifications and complexities of the CT mechanism, it is challenging to experimentally explore a library of donor−acceptor (D−A) blends to reach the optimum interface.

To date, fullerene derivatives [i.e., [6,6]-phenyl-C61-butyric acid methyl ester (PCBM)] as electron acceptors are frequently implemented in high-performing OPV devices.[16] However, the intrinsic deficiencies of fullerene-based acceptors, such as difficulty to tune energy levels, weak visible light absorption, and inherent tendency of easy aggregation, hamper their improvement for OPV devices.[17−19] Thus, non-fullerene acceptors, with synthetic flexibility and great potential to mitigate the aforementioned drawbacks of the fullerene acceptors are proposed as an alternative used in BHJ.[13] Non-fullerene acceptors have recently attracted a lot of attention from researchers in the development of BHJ organic solar cells. It has been hypothesized that under equal conditions, a BHJ involving non-fullerene acceptor will provide higher efficiency of CT. Therefore, a critical prerequisite and comparative exploration are required to be implemented at the fundamental electronic level for both fullerene and non-fullerene CP blends to unravel the reason behind differences in the relaxation pathways and CT rate at the interface. Hence, developing a computational framework to characterize/rank CT rate at the interface of different D−A blends would be noticeably advantageous for the community.

To address this, the underlying electronic ground state and formation of photo-induced CT at the interface need to be formulated.[20] Computationally efficient and precise density functional theory (DFT) techniques can be implemented to first explore the electronic structure of D−A blends.[21−23] Having DFT to provide optimized electronic states at the interface,[24] ab initio excited-state dynamics simulations can be

Received: March 8, 2022
Revised: June 29, 2022
Published: July 14, 2022

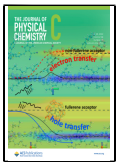

implemented next to probe the mechanisms behind experimentally measured CT rates.[25] The dynamics of charge carriers are often taken into account based on the reduced density matrix presented by the Redfield theory.[26] Then, the nonadiabatic couplings are performed to parametrize Redfield equations, from an on-the-fly coupling of the electron to lattice by the molecular dynamics (MD) trajectory developed upon DFT.[27] Recently, this methodology has been successfully applied to investigate nonradiative relaxation dynamics of perovskite PVs[28−30] and silicon surfaces.[31] Hence, in this work, we employ this paradigm to investigate the CT at the interface of CPs with fullerene and non-fullerene acceptor units, seeking a materials-by-design framework to computationally narrow down the list of candidate interfaces for BHJ of OPVs.

In this work, we employ nonadiabatic MD to investigate photo-induced CT of the diketopyrrolopyrrole (DPP)-based polymer[32] as a blend with non-fullerene (ITIC) and fullerene (PCBM) acceptor units. We study the non-radiative relaxation of photoexcited electrons and holes. Nonadiabatic couplings between electronic orbitals are computed based on nuclear trajectories obtained from ab initio calculations. We calculate the CT rates of charge carriers over time, where the difference between the CT of electron and hole can qualitatively represent the current density at zero voltage. The measurement of current density at the interface of different blends is utilized to qualitatively characterize the PCE. Our study illustrates the potential of the present computational methodology to explore the performance of D−A candidates for the next generation of OPV devices.

METHODS

Theoretical methods are logically organized into three sections: ground state DFT, nonadiabatic calculations, and computational details.

Ground State DFT. In this study, the atomic model is represented by the initial position of each ion, $\vec{R}_I$. The electronic structure is then determined through the solution of the self-consistent equation of DFT[33] via Vienna Ab initio Simulation Package (VASP).[34] This approach is established based on a fictitious one-electron Kohn−Sham (KS) equation

$$\left(-\frac{\hbar^2}{2m}\nabla^2 + \sum_I Z_I/(\vec{r} - \vec{R}_I) + v[\vec{r},\rho(\vec{r})]\right)\varphi_i^{\mathrm{KS}}(\vec{r}) = \varepsilon_i\varphi_i^{\mathrm{KS}}(\vec{r}) \tag{1}$$

where $\rho(\vec{r})$ stands for electronic charge distribution, and $\varphi_i^{\mathrm{KS}}(\vec{r})$ are KS orbitals with the orbital energy ε_i. The solution of the KS equations is single-electron KS orbitals that depend on the spatial variables $\varphi_i^{\mathrm{KS}}(\vec{r})$. Here, $v[\vec{r},\rho(\vec{r})]$ stands for exchange correlation potential and Z_I is the charge of ion I.

The total density of electrons $\rho(\vec{r})$ is calculated by a combination of the orbitals and orbital occupation function f_i.

$$\rho(\vec{r}) = \sum_{i,j} \rho_{i,j}^{\mathrm{eq}} \varphi_i^{\mathrm{KS}^*}(\vec{r})\varphi_j^{\mathrm{KS}}(\vec{r}) \tag{2}$$

where

$$\rho_{i,j}^{\mathrm{eq}} = \delta_{ij}f_i \,\&\, f_i = \begin{cases} 1, & i \le \mathrm{HOMO} \\ 0, & i \ge \mathrm{LUMO} \end{cases} \tag{3}$$

Here, HOMO and LUMO stand for highest occupied molecular orbital and lowest unoccupied molecular orbital, respectively. The electron density $\rho(\vec{r})$ is refined until reaching total energy convergence.

In the case of hybrid functionals, the HSE functional takes advantage of the fraction of Fock exchange, a, at zero electron separation and a length scale, $1/\omega$, where the short-range Fock exchange is computed as follows

$$E_{\mathrm{XC}}^{\mathrm{HSE}} = aE_{\mathrm{XC}}^{\mathrm{HF,SR}}(\omega) + (1-a)E_{\mathrm{X}}^{\mathrm{PBE,SR}}(\omega) + E_{\mathrm{X}}^{\mathrm{PBE,LR}}(\omega) + E_{\mathrm{X}}^{\mathrm{PBE}} \tag{4}$$

The short-range Fock exchange is then calculated via the spinful KS density matrix $\rho_{\sigma,\sigma'}(r, r')$[21]

$$E_{\mathrm{XC}}^{\mathrm{HF,SR}}(\omega) = -\frac{1}{2}\sum_{\sigma,\sigma'}\int \mathrm{d}r\mathrm{d}r' \frac{erfc(\omega|r-r'|)}{|r-r'|} \times |\rho_{\sigma,\sigma'}(r, r')|^2 \tag{5}$$

while the long-range and remaining short-range exchange are determined from the exchange-hole formulation of Perdew−Burke−Ernzerhof (PBE) functionals.[23]

The absorption spectra of the models are calculated based on the independent orbital approximation[35] and formulated as the summation of partial contribution

$$\alpha(\omega) = \sum_{ij} f_{ij}\delta(\hbar\omega - |\varepsilon_i - \varepsilon_j|) \tag{6}$$

where f_{ij} is the oscillator strength between states i and j

$$f_{ij} = \frac{4\pi m_e\omega_{ij}}{3he^2}|\vec{D}_{ij}|^2 \tag{7}$$

Here, $\langle\vec{D}_{ij}\rangle$ stands for the transition dipole moment

$$\langle\vec{D}_{ij}\rangle = \int \varphi_i^{\mathrm{KS}}\vec{r}\ \varphi_j^{\mathrm{KS}}\ \mathrm{d}\vec{r} \tag{8}$$

The probability of electronic transition between states i and j corresponding to the angular frequency ω of the incident light, indicates the oscillator strength. The transition dipole correlates the spatial overlap between pair of electronic states i and j and implies the matrix elements of the position operator. The delta function in equation eq 6 is approximated as a Lorentzian distribution to account for thermal fluctuations.

Density of states (DOS) is computed by counting the number of energy states that are available per energy interval and is computed as follows

$$n(\varepsilon) = \sum_i \delta(\varepsilon - \varepsilon_i) \tag{9}$$

where $n(\varepsilon)$ is the DOS, ε is an argument, ε_i stands for the energy of the ith KS orbital, and $\delta(\varepsilon - \varepsilon_i)$ is a Dirac delta function modeled based on a finite-width Lorentzian distribution to provide broadening due to thermal fluctuations.

Nonadiabatic Calculations. To explore CT dynamics at the interface of the CP and acceptor unit, we utilize ab initio MD with nonadiabatic couplings between nuclear and electronic degrees of freedom where the couplings provide dissipative transitions.[25,36−38] The nonadiabatic couplings are used to parameterize the Redfield theory[26] for the dynamics of the excited state. Then, dissipative electronic transitions are

https://doi.org/10.1021/acs.jpcc.2c01640
J. Phys. Chem. C 2022, 126, 12015−12024

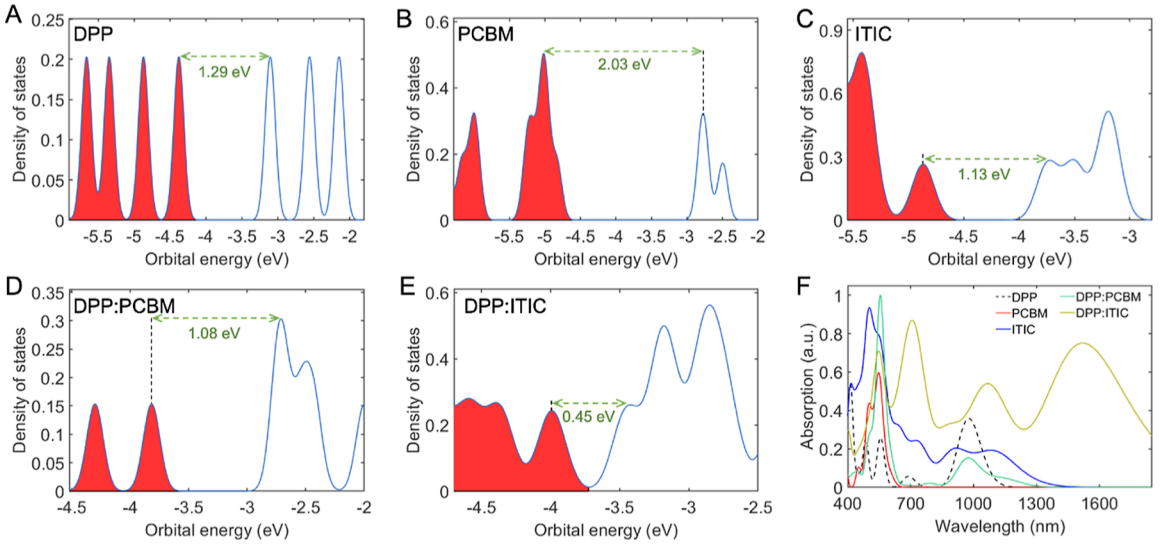

Figure 1. (A) DOS of the DPP polymer model. Red shaded regions indicate the occupied orbitals and unshaded regions represent unoccupied orbitals. (B) DOS's of the PCBM standalone unit, (C) ITIC standalone unit, (D) DPP:PCBM blend, and (E) DPP:ITIC blend. (F) Absorption spectrum of the DPP polymer, acceptor units, and blends. Ground-state calculations are performed via HSE06 functionals. Green arrows indicate band gap.

implemented to propagate the time evolution of the density matrix $\frac{d\rho_{ij}}{dt}$

$$\frac{d\rho_{ij}}{dt} = \frac{-i}{\hbar}\sum_{k}(F_{ik}\rho_{kj} - \rho_{ik}F_{kj}) + \left(\frac{d\rho_{ij}}{dt}\right)_{diss} \tag{10}$$

where F_{ik} stands for matrix element of the KS Hamiltonian and term $\left(\frac{d\rho_{ij}}{dt}\right)_{diss}$ provides electronic energy dissipation due to a heat bath generated by electron−phonon interactions. The iterative solution of eq 10 along the MD trajectory calculates dynamic charge density distribution, rate of transitions between electronic states with corresponding orbital energy ε_i, and rate of CT at the interface. The non-equilibrium charge distribution as a function of time and energy is calculated as follows

$$n^{(a,b)}(\varepsilon, t) = \sum_{i}\rho_{ii}^{(a,b)}(t)\delta(\varepsilon - \varepsilon_i) \tag{11}$$

where $n^{(a,b)}(\varepsilon,t)$ stands for the non-equilibrium charge distribution and (a,b) corresponds to the initial photo-excitation from state a to b, chosen based on the value of oscillator strength. The change in occupancy of electronic state populations from the equilibrium distribution is characterized by

$$\Delta n^{(a,b)}(\varepsilon, t) = n^{(a,b)}(\varepsilon, t) - n^{equil}(\varepsilon) \tag{12}$$

where $n^{equil}(\varepsilon)$ stands for the equilibrium charge distribution. The $\Delta n > 0$ describes the population gain and $\Delta n < 0$ indicates the population loss. Employing eq 12 to track the occupation of KS orbitals over time, the changes in charge distribution, as a function of z-coordinates, can be tracked as

$$\Delta n_{CB}^{(a,b)}(z, t) = \sum_{i,j\in CB}\rho_{ij}(t)\int dx\int dy(\varphi_i^*(\vec{r})\varphi_j(\vec{r})) \tag{13}$$

$$\Delta n_{VB}^{(a,b)}(z, t) = \sum_{i,j\in VB}\rho_{ij}(t)\int dx\int dy(\varphi_i^*(\vec{r})\varphi_j(\vec{r})) \tag{14}$$

where the KS orbitals are projected onto the z-axis by integrating over x- and y-components. The energy expectation values of hot electrons (the same way for the holes) are given by

$$\langle\Delta\varepsilon_e\rangle(t) = \sum_{i\geq LU}\rho_{ii}(t)\varepsilon_i(t) \tag{15}$$

The eq 15 equation can be rewritten in the dimensionless form of energy

$$\langle E_e\rangle(t) = \frac{\langle\Delta\varepsilon_e\rangle(t) - \langle\Delta\varepsilon_e\rangle(\infty)}{\langle\Delta\varepsilon_e\rangle(0) - \langle\Delta\varepsilon_e\rangle(\infty)} \tag{16}$$

To calculate the rates of charge carrier relaxation to band edges, the energy expectation value is converted into dimensionless energy, and energy relaxation is fitted to a single-exponential decay to solve for the rate constant[30]

$$k_e = \left\{\int_0^\infty \langle E_e\rangle(t)\,dt\right\}^{-1} \tag{17}$$

Next, the expectation value of hot electron and hole position in the space can be calculated as follows

$$\langle z^e\rangle(t) = \int dz\Delta n_{CB}^{(a,b)}(z, t)z \tag{18}$$

$$\langle z^h\rangle(t) = \int dz\Delta n_{VB}^{(a,b)}(z, t)z \tag{19}$$

where in the dimensionless form, we have

$$\langle Z^e\rangle(t) = \frac{\langle z^e\rangle(t) - \langle z^e\rangle(\infty)}{\langle z^e\rangle(0) - \langle z^e\rangle(\infty)} \tag{20}$$

$$\langle Z^h\rangle(t) = \frac{\langle z^h\rangle(t) - \langle z^h\rangle(\infty)}{\langle z^h\rangle(0) - \langle z^h\rangle(\infty)} \tag{21}$$

Finally, the total charge of the dipole over time is

https://doi.org/10.1021/acs.jpcc.2c01640
J. Phys. Chem. C 2022, 126, 12015−12024

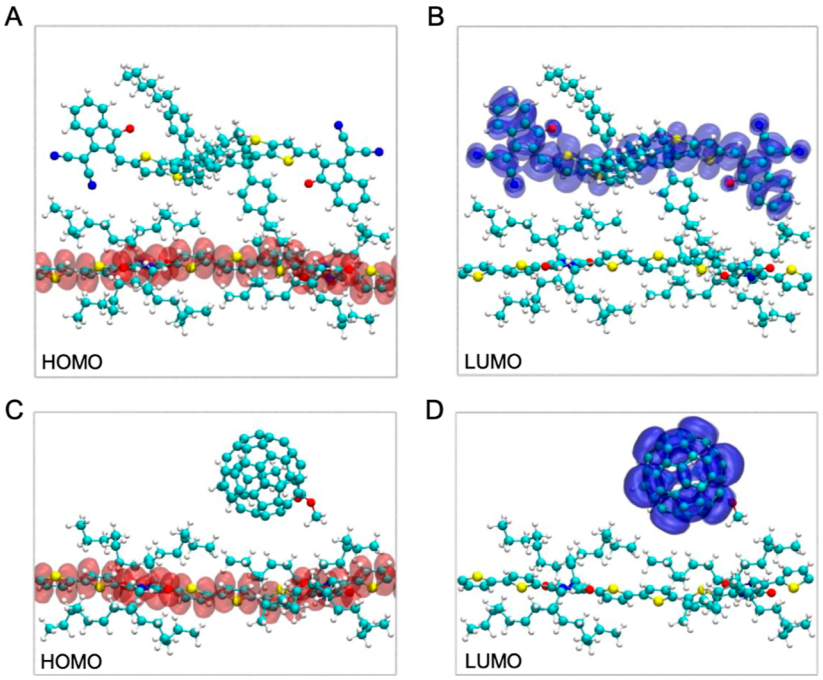

Figure 2. Partial charge density distribution of the HOMO and LUMO orbitals at the ground state: (A) Orbital of HOMO for DPP:ITIC. (B) Orbital of LUMO for DPP:ITIC. (C) Orbital of HOMO for DPP:PCBM. (D) Orbital of LUMO for DPP:PCBM. Shaded areas indicate the electron density. Calculations are performed via HSE06 functionals.

$$\langle \Delta Z \rangle(t) = \langle Z^{e} \rangle(t) - \langle Z^{h} \rangle(t) \tag{22}$$

The derivative of the total charge of the dipole over time indicates the current density that flows through the interface

$$\text{current density}(t) = j(t) = \frac{\mathrm{d}}{\mathrm{d}t} \langle \Delta Z \rangle(t) \tag{23}$$

where the maximum results of the current density $j(t)$ over time are considered here to characterize the CT at the interface.

Computational Details. The periodic model of CP consists of the two monomers, which are connected upon approximately 180° rotation relative to each other. This orientation is chosen to make adjacent thiophene groups more stable and preserve the linear structure of the backbone, while the same-oriented successive monomers indicate the curvature of the backbone within the conjugated plane.[39] The chemical structures of CP and acceptors are generated by the Materials Studio package and pre-optimized via force field calculations. The backbone of the CP is stretched in the y-direction. The side chains of C_6H_{13} and C_8H_{17} are grafted to both sides of the monomer. The pre-optimized structures of the acceptor units are located next to the CP in the *z*-direction. Before running dynamic calculations, all models are optimized by VASP to reach the ground state. For dynamics, all models are heated to a thermostat followed by MD simulations at 300 K. All simulations are performed via gamma point calculations. It should be noted that our nonadiabatic calculations are computed as an average over micro canonical ensemble where MD trajectories are sampled at several hundreds of time steps to ensure representation of as many possible states that the real system might experience. Indeed, we couple electronic and nuclear degrees of freedom with adiabatic MD simulations and calculate nonadiabatic couplings between adiabatic states using an "on-the-fly" procedure. All ab initio MD simulations of our atomic models are performed based on PBE functionals using plane-wave basis sets.

RESULTS

The DOS and the band structures of the ground states of the acceptor units and the CP blends are reported in Figure 1. To predict the band gap which has significant importance in PV-related applications, HSE06 functional is utilized to evaluate the electronic configuration of the system. The DOS in the vicinity of the gap of DPP is exhibited in Figure 1A, where a band gap of 1.29 eV is predicted, in good agreement with the reported experimental band gap of 1.3 eV,[40] implying that HSE06 functional appropriately predicts the ground state electronic structure of the DPP. For the PCBM and ITIC acceptor units, a band gap of 2.03 and 1.13 eV is predicted, respectively, see Figure 1B,C. Furthermore, as shown in Figure 1D, the DPP:PCBM blend shows a band gap of 1.08 eV indicating the addition of PCBM acceptor units to the DPP polymer improves charge mobility ended in a lower band gap comparing to pure DPP system. In the same manner for the DPP:ITIC blend, Figure 1E, a band gap of 0.45 eV is predicted, much smaller than the calculated value for DPP:PCBM blend. This implies that ITIC has better potential to tune/lower the band gap of the DPP polymer.

The corresponding wavelength of fundamental absorption of semiconductors usually occurs in the visible and near IR spectral range. We evaluate the absorption spectra, Figure 1F, to explore the influence of the acceptor unit on the absorbance of the DPP polymer. For the pure DPP, the maximum absorbance (λ_p) appears around 979 nm, larger than the observed experimental value of $\lambda_p \approx 800$ nm.[41] Despite utilizing the HSE06 functional, a considerable divergence to the experimental data is still observed. In our previous paper,[24] we showed that for such a 1D model, one needs to employ some numerical treatments such as *k*-point sampling to

https://doi.org/10.1021/acs.jpcc.2c01640
J. Phys. Chem. C 2022, 126, 12015−12024

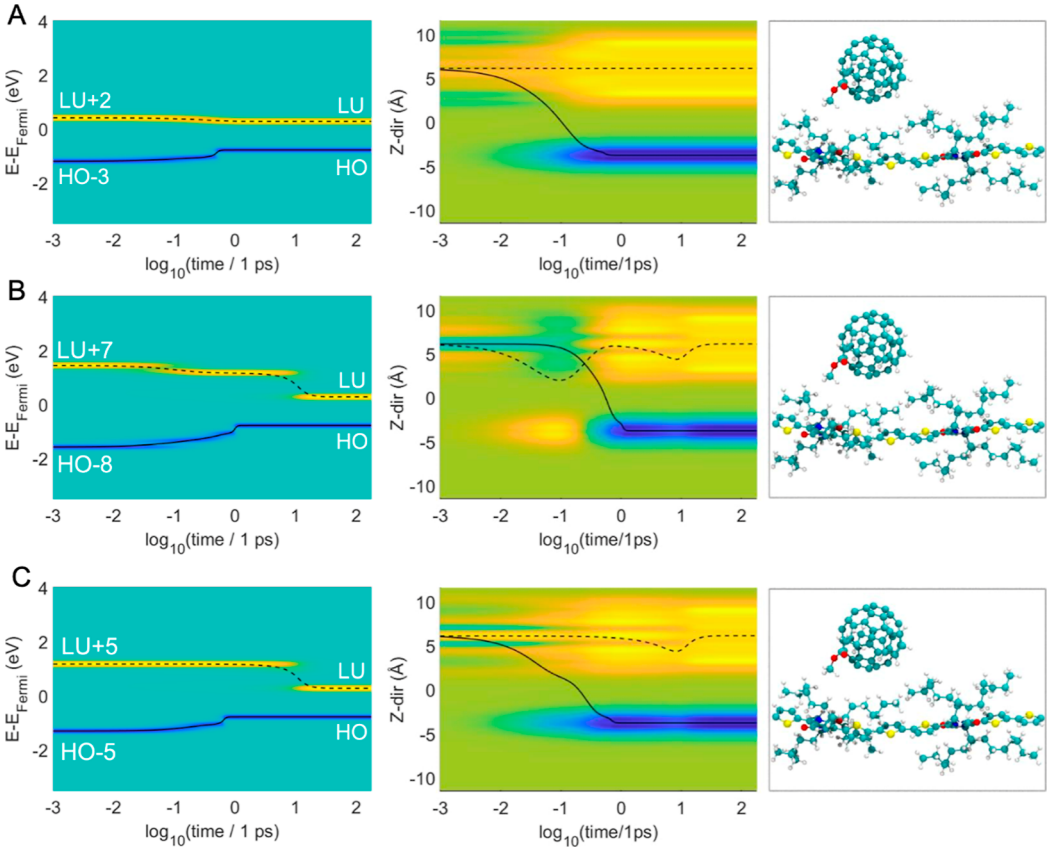

Figure 3. Charge carrier dynamics of the DPP:PCBM blend upon photoexcitation for three representative initial transitions which possess higher oscillator strength; (A) HO − 3 → LU + 2, (B) HO − 8 → LU + 7, and (C) HO − 5 → LU + 5. For all initial transitions, both excited electron and hole are located on PCBM. The left panels indicate the distribution of charge as a function of energy and time. Dashed and solid lines indicate expectation values for energy, calculated in an energy space distribution for conduction and valence bands, respectively. Middle panels represent charge density distribution as a function of time and position in the space. Electrons, equilibrium distribution, and holes are represented in yellow, green, and blue, respectively. The offset between solid and dashed lines corresponds to the electric dipole. The periodic cell is shown in the right panels where the PCBM acceptor is located at the top and the DPP polymer at the bottom.

mitigate the discrepancy between the computational results and experimental data. As it is shown in Figure 1F, ITIC shows stronger absorbance compared to the PCBM unit in agreement with experimental observations.[13] Accordingly, for both DPP:PCBM and DPP:ITIC, a red-shifted trend in the absorption spectrum is observed, where the DPP:ITIC blend exhibits much larger absorption which no longer remains in the visible/near IR spectral range and shifts into the IR region. Jiang and co-workers[42] experimentally measured a broad photo-response from 300 to 900 nm for a DPP:ITIC solar cell. Our DFT calculations highlight the higher potential of the ITIC to extend the absorption spectrum of the DPP polymer into the red and near-IR range, close to solar radiation emitted by the sun at sea level.

The calculated ground state partial charge densities of the HOMO and LUMO KS orbitals are shown in Figure 2, where the HSE06 functional is employed for the DFT calculations. For the DPP:ITIC blend, Figure 2A, the partial charge density of the HOMO orbital resides in the DPP backbone and this delocalized conjugated state is found to be conductive. Interestingly, the LUMO orbital of DPP:ITIC, Figure 2B, shows up on the ITIC acceptor unit, again delocalized through the backbone. The appearance of the HOMO on the donor and LUMO on the acceptor unit unravels the CT potential in the blend at the lower excitations. Indeed, HOMO and LUMO are considered to characterize interface energetics because these levels essentially govern charge transport and optical excitations. In the same manner for DPP:PCBM, HOMO orbital appears on the DPP backbone with a delocalized-conductive behavior, see Figure 2C. Accordingly, as exhibited in Figure 2D, the LUMO orbital resides on the PCBM acceptor unit which depicts the CT potential of the DPP:PCBM blend.

Figure 3 indicates three representative charge carrier dynamics upon photoexcitation for specific initial electronic transition for the DPP:PCBM interface with zero external electric fields. The initial transition is an instantaneous photoexcitation, which promotes a system to a non-equilibrium state by creating a hole in an initially occupied orbital and promoting an electron to an unoccupied orbital of the model. In the present study, selected transitions are characterized by high values of oscillator strengths, which are more probable to occur. All three considered transitions, Figure 3A−C, indicate that hole relaxation is faster than electron relaxation, and at the end of relaxation, hot electron relaxes on the PCBM acceptor unit and hot hole resides on the backbone of the DPP model. For this blend, all initial excitations start literally at PCBM, for both electron and hole. Furthermore, for the initial excitation of HO − 8 → LU + 7, Figure 3B, during the initial stage of dynamics, the electron temporarily transfers to the DPP. At the later time of relaxation, the electron returns back to the PCBM; however,

https://doi.org/10.1021/acs.jpcc.2c01640
J. Phys. Chem. C 2022, 126, 12015−12024

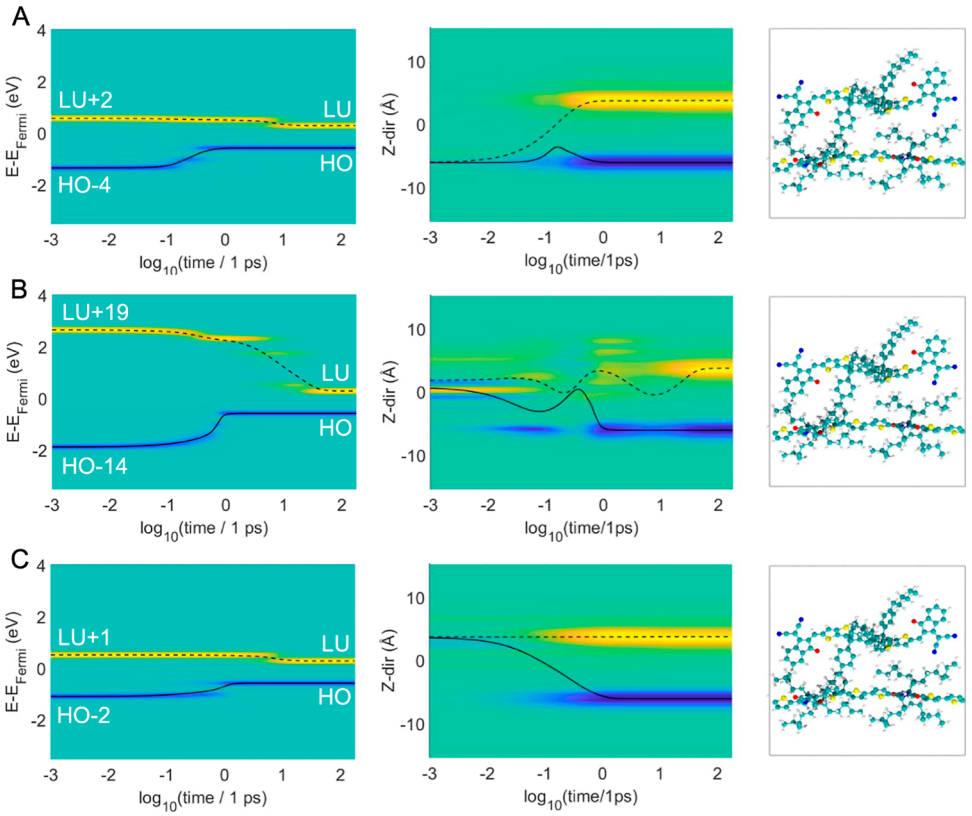

Figure 4. Charge carrier dynamics of the DPP:ITIC blend upon photoexcitation for three representative initial transitions which possess higher oscillator strength; (A) HO − 4 → LU + 2, (B) HO − 14 → LU + 19, and (C) HO − 2 → LU + 1. For panel A, initial excitation appears on DPP and for panels B and C initial excitation is observed on the ITIC unit. The left panels indicate the distribution of charge as a function of energy and time. Dashed and solid lines indicate expectation values for energy, calculated in an energy space distribution for conduction and valence bands, respectively. Middle panels represent charge density distribution as a function of time and position in the space. Electrons, equilibrium distribution, and holes are represented in yellow, green, and blue, respectively. The offset between solid and dashed lines corresponds to the electric dipole. The periodic cell is shown in the right panels where the ITIC acceptor is located at the top and DPP polymer at the bottom.

Table 1. Values of Transition Energy, Wavelength, Electron and Hole Cooling Rate (k_e and k_h), Maximum Current Density, and Averaged Values of Current Density at Different Initial Transitions of DPP:PCBM and DPP:ITIC Interfaces[a]

interface	initial transition	transition energy (eV)	wavelength λ (nm)	k_e (1/ps)	k_h (1/ps)	maximum current density $j(t)$
DPP:PCBM	HO − 3 → LU + 2	1.720	720.9	2.98	2.88	8.47
	HO − 8 → LU + 7	2.937	422.2	0.12	1.89	19.08
	HO − 5 → LU + 5	2.686	461.5	0.09	2.41	9.56
	average values (std)			1.06 (1.66)	2.39 (0.49)	12.37 (5.83)
DPP:ITIC	HO − 4 → LU + 2	1.831	677.2	0.17	3.31	12.93
	HO − 14 → LU + 19	4.655	266.35	0.09	1.77	26.75
	HO − 2 → LU + 1	1.410	879.2	0.14	1.49	5.96
	average values (std)			0.13 (0.04)	2.19 (0.98)	15.21 (10.58)

[a]The maximum instantaneous value of the current density is achieved for the DPP:ITIC interface, ∼1.4 times larger than the one for DPP:PCBM.

such "swinging" of electron back and forth could be potentially undesirable for practical PV applications.

Figure 4 shows three representative charge carrier dynamics upon photoexcitation for the DPP:ITIC blend. The distribution of charge as a function of time and energy following the initial photoexcitation from HO − 4 → LU + 2, Figure 4A, shows that the hole relaxation is much faster than electron relaxation. As it is demonstrated, the hole relaxes after around 0.7 ps, while the electron relaxation process starts after around 1.35 ps. The description of the charge carrier dynamics in space and time for the blend shows that the electron relaxes on the ITIC and holes are concentrated on the DPP backbone. The hot charge carrier dynamics for the HO − 14 → LU + 19, Figure 4B, transition is plotted where charge distribution declares the electron relaxation takes place between 31 and 63 ps, while the corresponding value for hole relaxation lies around 1 ps. After complete relaxation, the plot of charge carrier dynamics description in the space shows the electron concentration on ITIC and hole concentration on DPP. For the HO − 2 → LU + 1 transition, the similar behavior is observed where the hole relaxes after 2 ps faster than electron relaxation. At this transition state, electrons reside on the ITIC while holes are concentrated on the DPP backbone. For all transitions of DPP:ITIC, initial excitations appear on both DPP and ITIC units, implying the potential of both of them to serve as light absorbers. All excitations show the initial

https://doi.org/10.1021/acs.jpcc.2c01640
J. Phys. Chem. C 2022, 126, 12015−12024

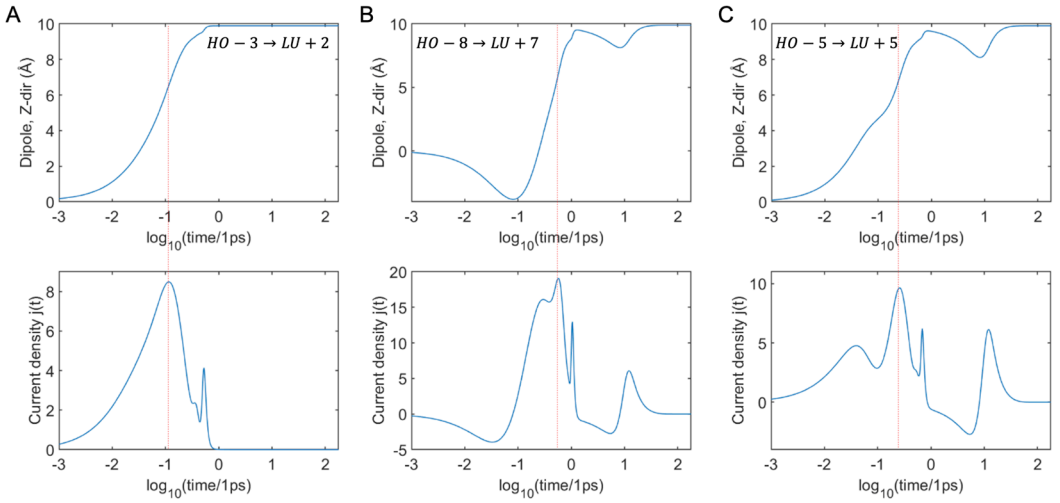

Figure 5. Dipole electric and current density of DPP:PCBM for three representative initial transitions; (A) HO − 3 → LU + 2, (B) HO − 8 → LU + 7, and (C) HO − 5 → LU + 5. The offset between the hot electron and hole expected position in the space corresponds to the electric dipole. Derivative of the total charge of the dipole over time indicates the current density.

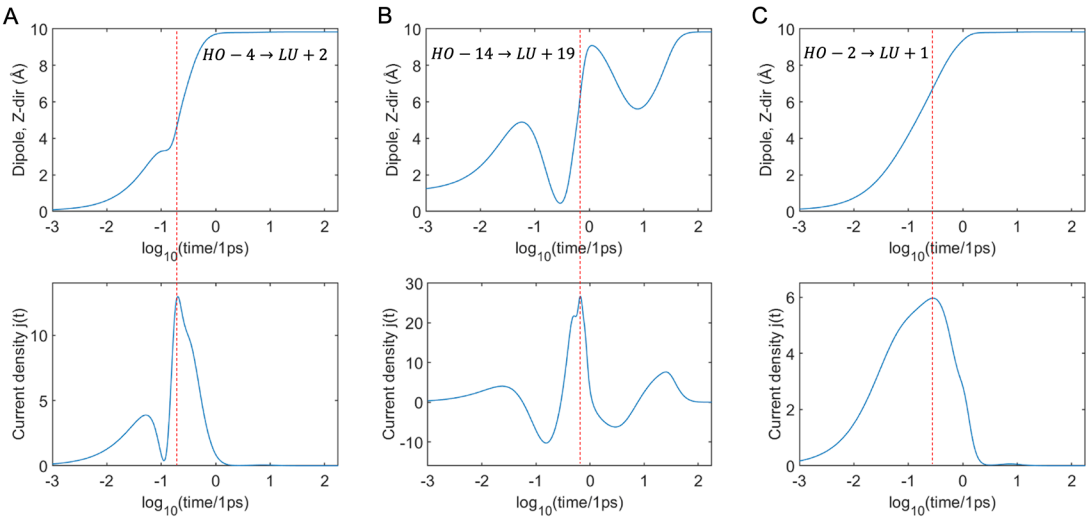

Figure 6. Dipole electric and current density of DPP:ITIC for three representative initial transitions; (A) HO − 4 → LU + 2, (B) HO − 14 → LU + 19, and (C) HO − 2 → LU + 1. The offset between the hot electron and hole expected position in the space corresponds to the electric dipole. Derivative of the total charge of the dipole over time indicates the current density.

electron−hole pair at ITIC, where the electron stays, while holes transfer to DPP. In this case, the swinging of electrons (back and forth) is less pronounced at the interface in comparison with DPP:PCBM.

Furthermore, to facilitate a better understanding of the CT between donor−acceptor units, we monitor the difference between expectation values of the spatial position of the charge carriers over time (i.e., electric dipole), and the results are reported in Table 1. These calculations unravel how quickly charge carriers are being separated. Generally, if the dipole values do not vary over time, no CT will happen at the interface and the blend would not be appropriate to be utilized in a PV device. By definition, the derivative of the dipole over time represents the current density. For the DPP:PCBM system, for the transition HO − 3 → LU + 2, Figure 5A, the inversed rate of the CT is observed at around 0.12 ps, which is an average time of transfer. It can be approximately assessed as the red line in Figure 5, the point where the dipole is making a halfway from the initial to the final value. For all transitions, the instant of time where half of the charge has been transferred through its way often coincides with the maximal derivative of the dipole (by definition reported as current density). For this transition, a maximum current density of 8.47 is computed. For the transition HO − 8 → LU + 7, Figure 5B, the inversed rate of the CT is calculated around 0.57 ps where the maximum current density of 19.08 is calculated. Eventually, HO − 5 → LU + 5 transition indicate the maximum current density of 9.56, see Figure 5A. A summary of dipole and maximum current density values is reported in Table 1. For the DPP:PCBM interface, those three selected initial transitions exhibit an average current density of 12.37.

The dipole and current density of DPP:ITIC blend over time are reported in Figure 6. As it is shown in Figure 6A, the transition HO − 4 → LU + 2 exhibits an inversed rate of the CT around 0.2 ps and a maximum current density of 12.93. For this transition, both DPP and ITIC can serve as efficient

https://doi.org/10.1021/acs.jpcc.2c01640
J. Phys. Chem. C 2022, 126, 12015−12024

light absorbers. The transition HO − 14 → LU + 19, Figure 6B, implies an inversed rate of the CT around 0.87 ps and maximum current density of 26.75. Finally, for the transition HO − 2 → LU + 1, Figure 6C, inversed rate of the CT is calculated around 0.29 ps, where maximum current density exhibits a value of 5.65. As summarized in Table 1, an averaged value of 15.21 is calculated for the three aforementioned transitions of the DPP:ITIC blend. This averaged current density value of the DPP:ITIC interface is higher than that 12.37 value of DPP:PCBM, implying the potential of the ITIC acceptor unit to provide more efficient CT than the PCBM unit.

DISCUSSION

Engineered interfaces between organic conjugated materials are of great importance for PV devices' function and efficiency where understanding the interface properties will facilitate the development of the next generation of OPVs. According to the previous studies, CPs as a blend with non-fullerene acceptor units indicate an improved PCE in BHJ solar cells compared to fullerene-based interfaces. Here, our first-principles calculations allow us to interpret both ground state static observables and dynamics CT at the interface of both non-fullerene and fullerene blends, at a fundamental electronic level. Under the same condition, the ITIC acceptor indicates stronger absorbance than PCBM, consequently, the combined absorbance of the DPP:ITIC captures preferable regions of the solar spectrum to achieve enhanced light-harvesting ability. The band gap of DPP:ITIC is found noticeably smaller than DPP:PCBM which is more favorable for OPVs because a smaller band gap maximizes PCE.

For the CPs as long-chain molecules, our results indicate the formation of delocalization HOMO orbital along with the conjugated backbone, which can form one-dimensional bands and facilitate the mobility of charge carriers. On the other hand, for the electron acceptors, a delocalized LUMO orbital on the ITIC unit similarly offers a preferable circumstance for the proper charge carriers' mobility, and interestingly, mobility is expected to contribute in mobility. This delocalized state on the ITIC fused-ring structure can easily form $\pi-\pi$ stacking with aromatic rings of the DPP's backbone (i.e., where the delocalized HOMO resides) which advantageously facilitates CT.[13] On the contrary, for the DPP:PCBM interface, despite the localization of the LUMO orbital on the buckyball of the PCBM unit, the cage-like fused-ring structure of the acceptor unit cannot provide an optimized interface (i.e., to facilitate CT) with DPP for the CT compared to ITIC. The organic BHJ devices need to possess an increased interface between the donor and acceptor for charge separation to address the limitations due to low exciton diffusion lengths in organic materials.[11,43−46] This increased area of interface between the donor and acceptor directly improves solar cell efficiencies suggesting a preferable charge separation throughout the BHJ.

For both DPP:PCBM and DPP:ITIC interfaces, non-adiabatic couplings indicate that electrons and holes have fast sub-picosecond carrier cooling. For all initial transitions, expectedly, the photoexcited electrons exhibit a long decay of hot carriers near the LUMO state. This is due to a large nonresonant subgap above the conduction band edge, and the transitions between electronic levels, experiencing a phonon bottleneck mechanism.[47,48] On the contrary, hole levels in the valence band are often spaced more densely and transition between electronic levels is quicker because there are a lot of nuclear phonon modes in resonance with them. A similar trend is observed by Hamada and Saeki,[49] in which time-resolved microwave conductivity measurements show a slower relaxation for the electrons compared to the holes in non-fullerene acceptor solar cells.

In addition, our calculations on the dynamics of charge carriers indicate that, under the same condition, changing the acceptor unit from PCBM to ITIC induces drastic qualitative changes in the pattern of CT at the interface of studied organic blends. There are three important observations from these dynamics calculations: (a) the amount of the charge transferred at the DPP:ITIC interface is higher than DPP:PCBM at several probable excitations scenarios, due to a more optimized interface to form $\pi-\pi$ stacking. (b) CT at the DPP:ITIC interface is more stable and the swinging of the charge carriers is less pronounced. (c) For the DPP:ITIC blend, the initial excitation observed on both donor and acceptor units, alternatively, and both DPP and ITIC can serve as light absorbers. For this blend, multiple channels of CT lead to a generation of charge separation as a prerequisite for efficient PV cells.

Eventually, despite the insightful observation of the charge carrier dynamics in this study, we want to discuss that the geometries of our current models are idealized to overcome the computational cost. Our challenging follow-up project will be developing condensed three-dimensional periodic models of organic BHJ to sample multiple CT interfaces between donor and acceptor units and enhance the reliability of the simulations. We believe packing multiple donor and acceptor units in a condensed simulation cell based on the experimentally recommended D−A weight ratio will provide more insightful computational models to explore CT.

CONCLUSIONS

In this study, we utilize DFT and density matrix theory to provide an insightful understanding of the optoelectronic properties of fullerene versus non-fullerene acceptors which are currently a major focus of the semiconductor's community. The key structure−property relationships and donor−acceptor matching properties are investigated. We explore the patterns of photo-induced CT of the DPP-based polymer as a blend with non-fullerene (ITIC) and fullerene (PCBM) acceptor units. The DPP:ITIC blend exhibits stronger near-IR absorption compared to the DPP:PCBM system. For both models, the partial charge density of the HOMO orbitals appears on the CP backbone, while for LUMO, it resides on the acceptor units, implying the potential for the donor−acceptor CT. The delocalized partial charges on both DPP (i.e., donor) and ITIC (i.e., acceptor unit) is preferable to from $\pi-\pi$ stacking and indicate a more favorable circumstance for the CT. The non-radiative dynamics of photoexcited charge carriers indicate that hole relaxation in energy and space is faster than electron relaxation. Furthermore, we establish a predictive computational framework to qualitatively characterize the PCE of different blends based on transfer rates of charge carriers over time, that is, difference between the transfer rate of electron and hole that represent the current density at zero voltage. CT rate calculations indicate that CP blend with ITIC offers a better PV effect compared to the PCBM-based blend. Our first-principles calculations indicate that for the DPP:ITIC system, CT is faster, swinging of charge carriers is less dominant, and both DPP and ITIC can serve as light absorbers. Our results demonstrate the efficacy of the

https://doi.org/10.1021/acs.jpcc.2c01640
J. Phys. Chem. C 2022, 126, 12015−12024

current approach as a computational design strategy to assess fundamental optoelectronic properties and CT capability of the newly designed donor−acceptor organic blends before any synthesis process, which would be advantageous for the development of the next generation of OPVs.

■ ASSOCIATED CONTENT

Supporting Information

The Supporting Information is available free of charge at https://pubs.acs.org/doi/10.1021/acs.jpcc.2c01640.

Computed absorption spectra of DPP:PCBM blend and DPP:ITIC blend models and atomistic coordinates of the optimized DPP:PCBM blend and DPP:ITIC blend models (PDF)

■ AUTHOR INFORMATION

Corresponding Authors

Wenjie Xia − *Department of Civil, Construction and Environmental Engineering, North Dakota State University, Fargo, North Dakota 58108, United States;* orcid.org/0000-0001-7870-0128; Email: wenjie.xia@ndsu.edu

Dmitri Kilin − *Department of Chemistry and Biochemistry, North Dakota State University, Fargo, North Dakota 58108, United States;* orcid.org/0000-0001-7847-5549; Email: dmitri.kilin@ndsu.edu

Author

Amirhadi Alesadi − *Department of Civil, Construction and Environmental Engineering, North Dakota State University, Fargo, North Dakota 58108, United States*

Complete contact information is available at: https://pubs.acs.org/10.1021/acs.jpcc.2c01640

Notes

The authors declare no competing financial interest.

■ ACKNOWLEDGMENTS

A.A. and W.X. acknowledge support from the National Science Foundation (NSF) under NSF OIA ND-ACES award no. 1946202. A.A. and W.X. acknowledge support from the North Dakota Established Program to Stimulate Competitive Research (ND EPSCoR) through the New Faculty Award, the Department of Civil, Construction and Environmental Engineering, and the College of Engineering at North Dakota State University (NDSU). The supercomputing resources of the National Energy Research Scientific Computing Center (NERSC), a U.S. Department of Energy Office of Science User Facility located at Lawrence Berkeley National Laboratory DOE, BES Chemical Sciences, NERSC contract no. DE-AC02-05CH11231, allocation award ERCAP0021557, "Computational Modeling of Photo-catalysis and Photo-induced CT Dynamics on Surfaces", and CCAST Thunder Cluster at NDSU are acknowledged. D.K. thanks DOE DE-SC0021287 for the exploration of 1D nanostructures similar to carbon nanotubes, NSF CHE 2004197 for the exploration of CT, and NSF CHE 1944921 for developing methods of quantum dynamics. D.K. thanks David Micha, Oleg Prezhdo, Sergei Tretiak, Svetlana Kilina, Andrei Zugayevich, Sebastian Alberti, Adrian Roitberg, and Tammie Nelson for inspiring discussions. Authors thank Yulun Han, David Graupner, Landon Johnson, Sarah Ghazanfari, and Kamrun Nahar Keya for editorial suggestions.

■ REFERENCES

(1) Mei, J.; Diao, Y.; Appleton, A. L.; Fang, L.; Bao, Z. Integrated Materials Design of Organic Semiconductors for Field-Effect Transistors. *J. Am. Chem. Soc.* **2013**, *135*, 6724−6746.

(2) Sirringhaus, H. 25th Anniversary Article: Organic Field-Effect Transistors: The Path beyond Amorphous Silicon. *Adv. Mater.* **2014**, *26*, 1319−1335.

(3) Sirringhaus, H.; Tessler, N.; Friend, R. H. Integrated Optoelectronic Devices Based on Conjugated Polymers. *Science* **1998**, *280*, 1741−1744.

(4) Zhang, S.; Alesadi, A.; Mason, G. T.; Chen, K. L.; Freychet, G.; Galuska, L.; Cheng, Y. H.; St. Onge, P. B. J.; Ocheje, M. U.; Ma, G.; Qian, Z.; Dhakal, S.; Ahmad, Z.; Wang, C.; Chiu, Y. C.; Rondeau-Gagné, S.; Xia, W.; Gu, X. Molecular Origin of Strain-Induced Chain Alignment in PDPP-Based Semiconducting Polymeric Thin Films. *Adv. Funct. Mater.* **2021**, *31*, 2100161.

(5) Zhang, S.; Alesadi, A.; Selivanova, M.; Cao, Z.; Qian, Z.; Luo, S.; Galuska, L.; Teh, C.; Ocheje, M. U.; Mason, G. T.; St. Onge, P. B. J.; Zhou, D.; Rondeau-Gagné, S.; Xia, W.; Gu, X.; Rondeau-Gagné, S.; Xia, W.; Gu, X.; Rondeau-Gagné, S.; Xia, W.; Gu, X. Toward the Prediction and Control of Glass Transition Temperature for Donor−Acceptor Polymers. *Adv. Funct. Mater.* **2020**, *30*, 2002221.

(6) Alesadi, A.; Cao, Z.; Li, Z.; Zhang, S.; Zhao, H.; Gu, X.; Xia, W. Machine Learning Prediction of Glass Transition Temperature of Conjugated Polymers from Chemical Structure. *Cell Rep. Phys. Sci.* **2022**, *3*, 100911.

(7) Zhan, X.; Zhu, D. Conjugated Polymers for High-Efficiency Organic Photovoltaics. *Polym. Chem.* **2010**, *1*, 409−419.

(8) Saito, M.; Ohkita, H.; Osaka, I. π-Conjugated Polymers and Molecules Enabling Small Photon Energy Loss Simultaneously with High Efficiency in Organic Photovoltaics. *J. Mater. Chem. A* **2020**, *8*, 20213−20237.

(9) Fan, B.; Li, M.; Zhang, D.; Zhong, W.; Ying, L.; Zeng, Z.; An, K.; Huang, Z.; Shi, L.; Bazan, G. C.; Huang, F.; Cao, Y. Tailoring Regioisomeric Structures of π-Conjugated Polymers Containing Monofluorinated π-Bridges for Highly Efficient Polymer Solar Cells. *ACS Energy Lett.* **2020**, *5*, 2087−2094.

(10) Li, Y. Molecular Design of Photovoltaic Materials for Polymer Solar Cells: Toward Suitable Electronic Energy Levels and Broad Absorption. *Acc. Chem. Res.* **2012**, *45*, 723−733.

(11) Yu, G.; Gao, J.; Hummelen, J. C.; Wudl, F.; Heeger, A. J. Polymer Photovoltaic Cells: Enhanced Efficiencies via a Network of Internal Donor-Acceptor Heterojunctions. *Science* **1995**, *270*, 1789−1791.

(12) Choi, J.; Kim, W.; Kim, S.; Kim, T. S.; Kim, B. J. Influence of Acceptor Type and Polymer Molecular Weight on the Mechanical Properties of Polymer Solar Cells. *Chem. Mater.* **2019**, *31*, 9057.

(13) Lin, Y.; Wang, J.; Zhang, Z.-G.; Bai, H.; Li, Y.; Zhu, D.; Zhan, X. An Electron Acceptor Challenging Fullerenes for Efficient Polymer Solar Cells. *Adv. Mater.* **2015**, *27*, 1170−1174.

(14) Yang, Y.; Zhang, Z. G.; Bin, H.; Chen, S.; Gao, L.; Xue, L.; Yang, C.; Li, Y. Side-Chain Isomerization on an n-Type Organic Semiconductor ITIC Acceptor Makes 11.77% High Efficiency Polymer Solar Cells. *J. Am. Chem. Soc.* **2016**, *138*, 15011−15018.

(15) Doumon, N. Y.; Dryzhov, M. V.; Houard, F. V.; Le Corre, V. M.; Rahimi Chatri, A.; Christodoulis, P.; Koster, L. J. A. Photostability of Fullerene and Non-Fullerene Polymer Solar Cells: The Role of the Acceptor. *ACS Appl. Mater. Interfaces* **2019**, *11*, 8310−8318.

(16) He, Y.; Li, Y. Fullerene Derivative Acceptors for High Performance Polymer Solar Cells. *Phys. Chem. Chem. Phys.* **2011**, *13*, 1970−1983.

(17) Zhao, W.; Qian, D.; Zhang, S.; Li, S.; Inganäs, O.; Gao, F.; Hou, J. Fullerene-free Polymer Solar Cells with over 11% Efficiency and Excellent Thermal Stability. *Adv. Mater.* **2016**, *28*, 4734−4739.

(18) Hou, J.; Inganäs, O.; Friend, R. H.; Gao, F. Organic Solar Cells Based on Non-Fullerene Acceptors. *Nat. Mater.* **2018**, *17*, 119−128.

(19) Yan, C.; Barlow, S.; Wang, Z.; Yan, H.; Jen, A. K.-Y.; Marder, S. R.; Zhan, X. Non-Fullerene Acceptors for Organic Solar Cells. *Nat. Rev. Mater.* **2018**, *3*, 1−19.

(20) Han, Y.; Micha, D. A.; Kilin, D. S. Ab Initio Study of the Photocurrent at the Au/Si Metal-Semiconductor Nanointerface. *Mol. Phys.* **2015**, *113*, 327−335.
(21) Moussa, J. E.; Schultz, P. A.; Chelikowsky, J. R. Analysis of the Heyd-Scuseria-Ernzerhof Density Functional Parameter Space. *J. Chem. Phys.* **2012**, *136*, 204117.
(22) Sholl, D.; Steckel, J. A. *Density Functional Theory: A Practical Introduction*; John Wiley & Sons, 2011.
(23) Perdew, J. P.; Burke, K.; Ernzerhof, M. Generalized Gradient Approximation Made Simple. *Phys. Rev. Lett.* **1996**, *77*, 3865.
(24) Alesadi, A.; Fatima, F.; Xia, W.; Kilin, D. First-Principles Study on the Electronic Properties of PDPP-Based Conjugated Polymer via Density Functional Theory. *J. Phys. Chem. B* **2021**, *125*, 8953−8964.
(25) Forde, A.; Kilin, D. Hole Transfer in Dye-Sensitized Cesium Lead Halide Perovskite Photovoltaics: Effect of Interfacial Bonding. *J. Phys. Chem. C* **2017**, *121*, 20113−20125.
(26) Redfield, A. G. On the Theory of Relaxation Processes. *IBM J. Res. Dev.* **1957**, *1*, 19−31.
(27) Hammes-Schiffer, S.; Tully, J. C. Proton Transfer in Solution: Molecular Dynamics with Quantum Transitions. *J. Chem. Phys.* **1994**, *101*, 4657−4667.
(28) Han, Y.; Kilin, D. S. Nonradiative Relaxation Dynamics of a Cesium Lead Halide Perovskite Photovoltaic Architecture: Effect of External Electric Fields. *J. Phys. Chem. Lett.* **2020**, *11*, 9983−9989.
(29) Forde, A.; Inerbaev, T.; Kilin, D. Spectral Signatures of Positive and Negative Polarons in Lead-Halide Perovskite Nanocrystals. *J. Phys. Chem. C* **2019**, *124*, 1027−1041.
(30) Forde, A.; Inerbaev, T.; Hobbie, E. K.; Kilin, D. S. Excited-State Dynamics of a CsPbBr3 Nanocrystal Terminated with Binary Ligands: Sparse Density of States with Giant Spin-Orbit Coupling Suppresses Carrier Cooling. *J. Am. Chem. Soc.* **2019**, *141*, 4388−4397.
(31) Han, Y.; Iduoku, K.; Grant, G.; Rasulev, B.; Leontyev, A.; Hobbie, E. K.; Tretiak, S.; Kilina, S. V.; Kilin, D. S. Hot Carrier Dynamics at Ligated Silicon(111) Surfaces: A Computational Study. *J. Phys. Chem. Lett.* **2021**, *12*, 7504−7511.
(32) Chen, H.; Guo, Y.; Yu, G.; Zhao, Y.; Zhang, J.; Gao, D.; Liu, H.; Liu, Y. Highly π-Extended Copolymers with Diketopyrrolopyrrole Moieties for High-Performance Field-Effect Transistors. *Adv. Mater.* **2012**, *24*, 4618−4622.
(33) Hohenberg, P.; Kohn, W. Inhomogeneous Electron Gas. *Phys. Rev.* **1964**, *136*, B864.
(34) Kresse, G.; Furthmüller, J. Efficient Iterative Schemes for Ab Initio Total-Energy Calculations Using a Plane-Wave Basis Set. *Phys. Rev. B: Condens. Matter Mater. Phys.* **1996**, *54*, 11169.
(35) Han, Y.; Meng, Q.; Rasulev, B.; May, P. S.; Berry, M. T.; Kilin, D. S.; Vogel, D. J.; Kryjevski, A.; Inerbaev, T.; Kilin, D. S.; Han, Y.; Meng, Q.; Rasulev, B.; May, P. S.; Berry, M. T.; Kilin, D. S. Photoinduced Charge Transfer versus Fragmentation Pathways in Lanthanum Cyclopentadienyl Complexes. *J. Chem. Theory Comput.* **2017**, *8*, 4281−4296.
(36) Chen, J.; Schmitz, A.; Kilin, D. S. Computational Simulation of the P-n Doped Silicon Quantum Dot. *Int. J. Quantum Chem.* **2012**, *112*, 3879−3888.
(37) Kilin, D. S.; Micha, D. A. Relaxation of Photoexcited Electrons at a Nanostructured Si (111) Surface. *J. Phys. Chem. Lett.* **2010**, *1*, 1073−1077.
(38) Han, Y.; Micha, D. A.; Kilin, D. S. Ab Initio Study of the Photocurrent at the Au/Si Metal−Semiconductor Nanointerface. *Mol. Phys.* **2015**, *113*, 327−335.
(39) Vezie, M. S.; Few, S.; Meager, I.; Pieridou, G.; Dörling, B.; Ashraf, R. S.; Goñi, A. R.; Bronstein, H.; McCulloch, I.; Hayes, S. C.; Campoy-Quiles, M.; Nelson, J. Exploring the Origin of High Optical Absorption in Conjugated Polymers. *Nat. Mater.* **2016**, *15*, 746−753.
(40) Bijleveld, J. C.; Zoombelt, A. P.; Mathijssen, S. G. J.; Wienk, M. M.; Turbiez, M.; de Leeuw, D. M.; Janssen, R. A. J. Poly (Diketopyrrolopyrrole− Terthiophene) for Ambipolar Logic and Photovoltaics. *J. Am. Chem. Soc.* **2009**, *131*, 16616−16617.
(41) Hofmann, A. I.; Kroon, R.; Zokaei, S.; Järsvall, E.; Malacrida, C.; Ludwigs, S.; Biskup, T.; Müller, C. Chemical Doping of Conjugated Polymers with the Strong Oxidant Magic Blue. *Adv. Electron. Mater.* **2020**, *6*, 2000249.
(42) Jiang, X.; Xu, Y.; Wang, X.; Wu, Y.; Feng, G.; Li, C.; Ma, W.; Li, W. Non-Fullerene Organic Solar Cells Based on Diketopyrrolopyrrole Polymers as Electron Donors and ITIC as an Electron Acceptor. *Phys. Chem. Chem. Phys.* **2017**, *19*, 8069−8075.
(43) Waldauf, C.; Scharber, M. C.; Schilinsky, P.; Hauch, J. A.; Brabec, C. J. Physics of Organic Bulk Heterojunction Devices for Photovoltaic Applications. *J. Appl. Phys.* **2006**, *99*, 104503.
(44) Halls, J. J. M.; Walsh, C. A.; Greenham, N. C.; Marseglia, E. A.; Friend, R. H.; Moratti, S. C.; Holmes, A. B. Efficient Photodiodes from Interpenetrating Polymer Networks. *Nature* **1995**, *376*, 498−500.
(45) Kannan, B.; Castelino, K.; Majumdar, A. Design of Nanostructured Heterojunction Polymer Photovoltaic Devices. *Nano Lett.* **2003**, *3*, 1729−1733.
(46) Haugeneder, A.; Neges, M.; Kallinger, C.; Spirkl, W.; Lemmer, U.; Feldmann, J.; Scherf, U.; Harth, E.; Gügel, A.; Müllen, K. Exciton Diffusion and Dissociation in Conjugated Polymer/Fullerene Blends and Heterostructures. *Phys. Rev. B: Condens. Matter Mater. Phys.* **1999**, *59*, 15346.
(47) Urayama, J.; Norris, T. B.; Singh, J.; Bhattacharya, P. Observation of Phonon Bottleneck in Quantum Dot Electronic Relaxation. *Phys. Rev. Lett.* **2001**, *86*, 4930.
(48) Kilina, S. V.; Neukirch, A. J.; Habenicht, B. F.; Kilin, D. S.; Prezhdo, O. V. Quantum Zeno Effect Rationalizes the Phonon Bottleneck in Semiconductor Quantum Dots. *Phys. Rev. Lett.* **2013**, *110*, 180404.
(49) Hamada, F.; Saeki, A. Mobility Relaxation of Holes and Electrons in Polymer:Fullerene and Polymer : Non-Fullerene Acceptor Solar Cells. *ChemSusChem* **2021**, *14*, 3528−3534.

https://doi.org/10.1021/acs.jpcc.2c01640
J. Phys. Chem. C 2022, 126, 12015−12024